PAPER • OPEN ACCESS

Non-equilibrium band broadening, gap renormalization and band inversion in black phosphorus

To cite this article: H Hedayat *et al* 2021 *2D Mater.* **8** 025020

View the article online for updates and enhancements.

2D Materials

PAPER

Non-equilibrium band broadening, gap renormalization and band inversion in black phosphorus

H Hedayat[1], A Ceraso[1,2], G Soavi[3,4], S Akhavan[4], A Cadore[4], C Dallera[2], G Cerullo[1,2], A C Ferrari[4] and E Carpene[1]

1 Institute of Photonics and Nanotechnologies IFN-CNR, Piazza Leonardo Da Vinci 32, Milano 20133, Italy
2 Dipartimento di Fisica, Politecnico di Milano, Piazza Leonardo da Vinci 32, Milano 20133, Italy
3 Institute for Solid State Physics, Abbe Center of Photonics, Friedrich-Schiller University Jena, 07743 Jena, Germany
4 Cambridge Graphene Centre, University of Cambridge, 9 JJ Thomson Avenue, Cambridge CB3 0FA, United Kingdom

E-mail: giulio.cerullo@polimi.it, acf26@eng.cam.ac.uk and ettore.carpene@polimi.it

Abstract

Black phosphorous (BP) is a layered semiconductor with high carrier mobility, anisotropic optical response and wide bandgap tunability. In view of its application in optoelectronic devices, understanding transient photo-induced effects is crucial. Here, we investigate by time- and angle-resolved photoemission spectroscopy BP in its pristine state and in the presence of Stark splitting, chemically induced by Cs ad-sorption. We show that photo-injected carriers trigger bandgap renormalization, and a concurrent valence band flattening caused by Pauli blocking. In biased samples, photo-excitation leads to a long-lived (ns) surface photovoltage of few hundreds mV that counterbalances the Cs-induced surface band bending. This allows us to disentangle bulk from surface electronic states, and to clarify the mechanism underlying the band inversion observed in bulk samples.

1. Introduction

Black phosphorous (BP) is a layered semiconductor with interesting physical properties, such as high carrier mobility (up to 10^4 cm^2 V^{-1} s^{-1} in the monolayer (1L)) [1], large electronic/optical anisotropies (reflectance and DC conductance can vary by a factor $\sim$2–4 with in-plane orientation) [2, 3] and excellent mechanical properties (1L-BP can sustain tensile strain up to $\sim$30%) [4]. Its direct bandgap depends on the number of layers [5, 6], ranging from $\sim$0.4 eV in bulk [7] to $\sim$2 eV in 1L-BP, phosphorene [5], and is sensitive to pressure [8, 9], electric field [10–13] and in-plane strain [14, 15]. References [16–18] demonstrated that surface doping by alkali atoms allows to engineer the gap of BP, leading to surface band inversion at a critical dopant concentration $\sim$0.4 1L ($\sim$9 × 10^{13} cm^{-2}) [16]. This gap tunability is attributed to the so-called giant Stark effect [19, 20], i.e. an electric field-induced shift of electronic states, named 'giant' since it can lead to gap closure, as confirmed by modeling [6, 10, 17, 18] and photoemission experiments [17, 21], along with a pronounced surface depletion at the valence band (VB) and a concurrent surface confinement of the conduction band (CB).

In light of the promise of BP for opto-electronic applications [2, 22, 23], it is important to understand its ultrafast non-equilibrium response. Time- and angle-resolved photoemission spectroscopy (TARPES), exploiting a pump-probe scheme, can track the dynamics of the electronic structure after an ultrashort (tens of fs) optical stimulus [24]. To date, only a few TARPES studies have been performed on BP. The role of photo-induced band broadening and ionized surface impurities on carrier dynamics was studied in Ref. [25], suggesting the absence of bandgap renormalization (BGR) [26, 27]. On the other hand, the VB shift triggered by optical excitation was attributed to BGR and corroborated by *ab-initio* calculations [28], in agreement with resonant transient absorption measurements [29]. Although extensive theoretical work was done on 1L- and few-layers (FL) BP [5, 6, 10–12, 14, 18], ARPES measurements were only performed on bulk crystals cleaved *in situ*, with no control on sample thickness [16, 17, 25, 28, 30]. The depth sensitivity of photoemission critically depends on the photon

energy $h\nu$ (it can range from 1L at $h\nu \sim 100$ eV to several nm at $h\nu \sim 6$ eV) [31]. ARPES cannot ignore the presence of underlying bulk states, and the comparison with 1L- or FL-BP theoretical predictions might be misleading.

Here we use TARPES with 6 eV probe photons to investigate the ultrafast response of photo-excited bulk BP, with and without a vertical electric bias, resulting from Cs adsorption, to trigger Stark splitting. Photo-injected electron (e)–hole (h) pairs thermalize within a few ps and induce VB broadening. By comparing the dynamics of pristine and alkali-adsorbed samples, we assign the broadening to carriers drift-diffusion processes, and not to the previously claimed Stark-related effects [25]. Our analysis also reveals ~ 50 meV BGR entwined to a transient VB flattening that arises from band filling. In biased BP, pump photons trigger surface photovoltage (SPV) of a few hundreds mV, in agreement with TARPES measurements at fixed pump-probe delay [32]. We demonstrate that SPV can partially or totally compensate Cs-induced band bending. The sensitivity of our experiment allows us to disentangle bulk from surface electronic states, and to establish that band inversion is a crossing between *surface* CB and *bulk* VB. Thus, the semiconductor-to-semimetal transition upon alkali surface doping can be argued only in 1L- or FL-BP [18], where bulk contributions are absent.

2. Results and discussion

BP crystallizes in the orthorhombic structure [7, 33], where sp^3 orbital hybridization leads to buckled layers normal to the z-axis, figure 1(a). In the bulk, the direct bandgap is located at the Z point of the first Brillouin Zone (BZ) [7], figure 1(b), and is strongly anisotropic, figure 1(c). The e/h effective masses range from $\sim 0.08 \times m_0$ along the x-axis (armchair direction, m_0 is the free electron mass) [7] to $\sim 1 \times m_0$ along the y-axis (zigzag direction) [7]. Here, we consider the armchair (x) direction, where band dispersion is largest (smallest effective mass), but our conclusions on band dynamics are unaffected by the in-plane crystallographic orientation because we probe the region surrounding the Z symmetry point.
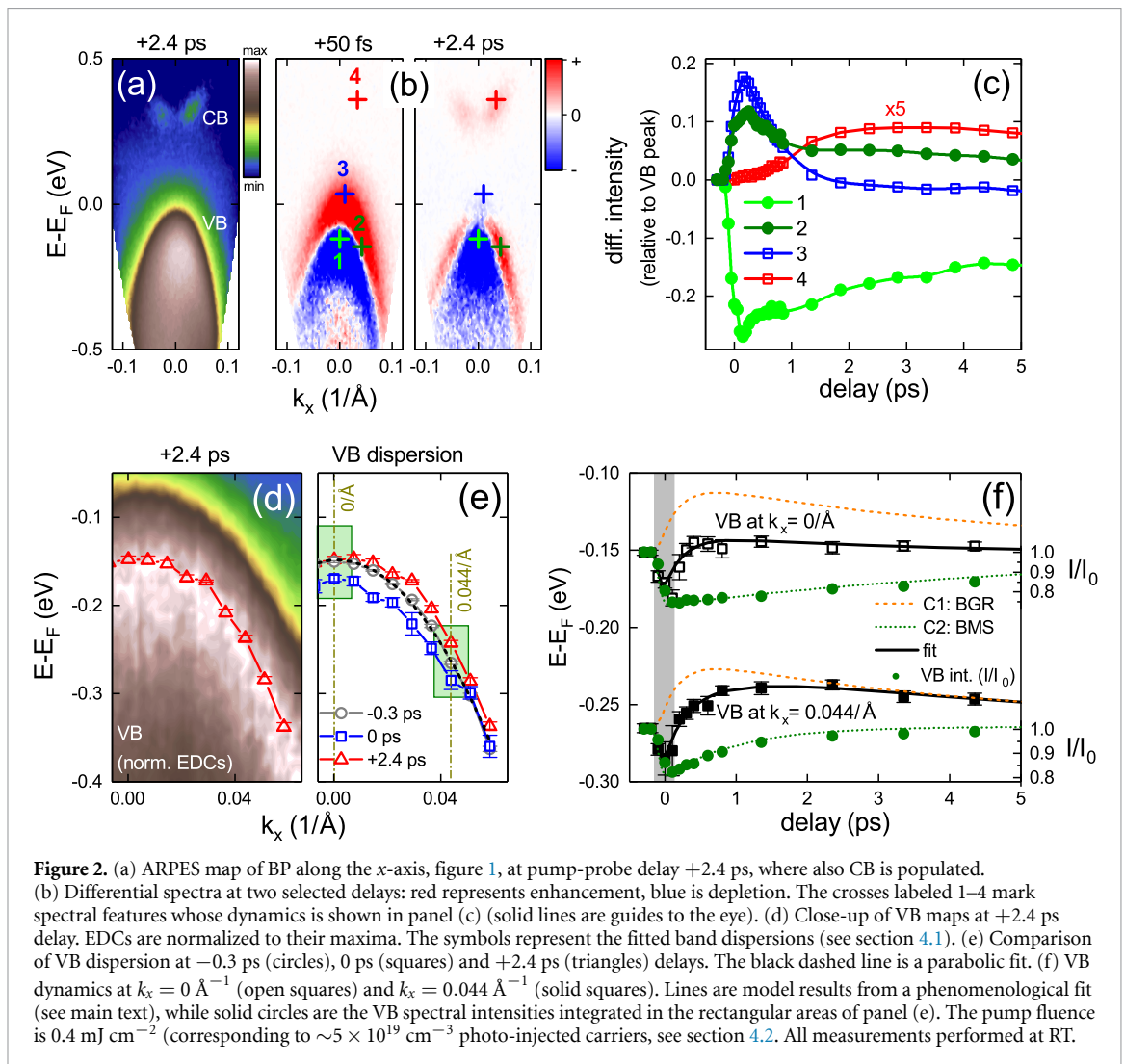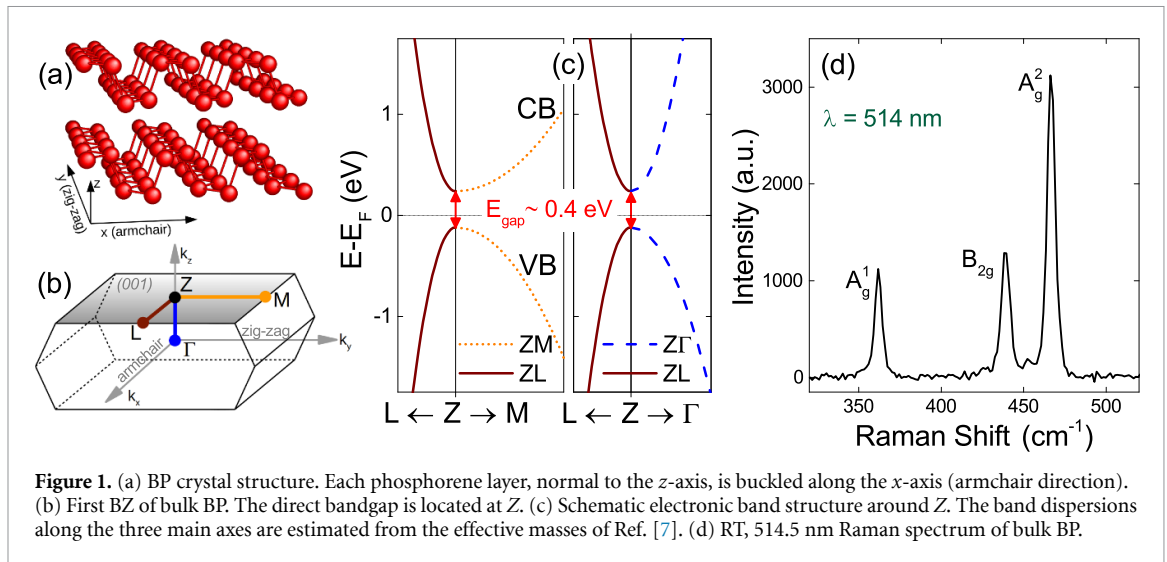
We use bulk BP from HQ graphene. Samples are characterized by Raman spectroscopy [34–36] utilizing a Renishaw InVia equipped with a $50\times$ objective (numerical aperture NA $= 0.75$) at 514 nm. The laser power is kept below 100 μW to avoid any possible damage [37]. Before measuring, the surface oxidized layer is pulled off via micromechanical cleavage by tape [38–40]. The Raman spectrum of BP exhibits three major peaks, as shown in figure 1(d). They correspond to in-plane B_{2g} and A_g^2, and out-of-plane A_g^1, vibrational modes [40, 41]. Our BP flakes show A_g^1, B_{2g} and $A_g^2 \sim 361.9$, 439.1, and 466.7 cm^{-1},

respectively, in good agreement with bulk BP literature [39–42].

TARPES is performed with the setup described in Ref. [43]. The laser source, based on a Yb system (Pharos, Light Conversion) and a non-collinear optical parametric amplifier, provides ultrashort pump ($h\nu = 1.82$ eV, pulse duration 30 fs) and probe ($h\nu = 6$ eV, pulse duration 70 fs) pulses at 80 kHz repetition rate. p-polarized pump and probe beams, focused respectively on spots ~ 135 and ~ 60 μm in diameter, impinge at $45°$ on the sample cleaved in-situ under ultrahigh vacuum conditions ($\sim 10^{-10}$ mbar). Photo-emitted e are detected by a hemispherical analyzer (Phoibos 100, Specs), with a combined energy resolution ~ 30 meV (as estimated from the low energy cut-off of the spectra, see section 4.1) and angular acceptance $\pm 15°$. All data are recorded at room temperature (RT). The in-plane crystallographic orientation of the sample is determined by Low Energy Electron Diffraction, and cross-checked by exploiting the in-plane anisotropy of the VB dispersion seen by ARPES.

Cs deposition is performed with a SAES Getters dispenser inside the preparation chamber adjacent the photoemission one [43]. The current through the dispenser (~ 5 A) is adjusted to keep $\sim 10^{-9}$ mbar during deposition (with starting pressure $\sim 10^{-10}$ mbar, see section 4.3). The doping dose, proportional to the deposition time, is estimated comparing the resulting bandgap with the data in Ref. [16]. This indicates that 45 s correspond to the critical dose ~ 0.35 1L Cs that closes the bandgap. Grazing incidence x-ray photoemission spectroscopy measurements in Ref. [17] showed that adsorbed Cs does not intercalate into BP.

Figure 2(a) shows the RT ARPES map of bulk BP along the armchair direction (see figure 1), following excitation by a 30 fs pulse at 1.82 eV. The map, recorded at a positive, i.e. after pump arrival, pump-probe delay of $+2.4$ ps, reveals also the normally unoccupied CB. Figure 2(b) reports the differential ARPES maps obtained subtracting the photoemission spectrum acquired before pump arrival from spectra at two selected pump-probe delays. Red color represents photo-induced increase of spectral weight, while blue represents depletion. The crosses labeled 1–4 in figure 2(b) mark relevant features (band extrema and sides), and their temporal evolution is reported in figure 2(c). While the VB (labels 1–3) shows a prompt (<100 fs) response to pump pulses, the CB (label 4) has a slow build-up, on the ps scale, indicating that it is *indirectly* populated: photo-excited e decay from higher energy levels reached by the excitation pulse toward the CB bottom via e–e [44] and e–phonon [45] scattering processes. Due to the bandgap, the enhanced intensity on the VB upper border (labels 2,3) is ascribed to photo-induced broadening and/or shift of the band edge. Such enhancement has a longer

Figure 1. (a) BP crystal structure. Each phosphorene layer, normal to the *z*-axis, is buckled along the *x*-axis (armchair direction). (b) First BZ of bulk BP. The direct bandgap is located at *Z*. (c) Schematic electronic band structure around *Z*. The band dispersions along the three main axes are estimated from the effective masses of Ref. [7]. (d) RT, 514.5 nm Raman spectrum of bulk BP.

Figure 2. (a) ARPES map of BP along the *x*-axis, figure 1, at pump-probe delay +2.4 ps, where also CB is populated. (b) Differential spectra at two selected delays: red represents enhancement, blue is depletion. The crosses labeled 1–4 mark spectral features whose dynamics is shown in panel (c) (solid lines are guides to the eye). (c) Close-up of VB maps at +2.4 ps delay. EDCs are normalized to their maxima. The symbols represent the fitted band dispersions (see section 4.1). (e) Comparison of VB dispersion at −0.3 ps (circles), 0 ps (squares) and +2.4 ps (triangles) delays. The black dashed line is a parabolic fit. (f) VB dynamics at $k_x = 0$ Å^{-1} (open squares) and $k_x = 0.044$ Å^{-1} (solid squares). Lines are model results from a phenomenological fit (see main text), while solid circles are the VB spectral intensities integrated in the rectangular areas of panel (e). The pump fluence is 0.4 mJ cm^{-2} (corresponding to $\sim 5 \times 10^{19}$ cm^{-3} photo-injected carriers, see section 4.2. All measurements performed at RT.

lifetime on the VB sides (label 2) compared to the VB center (label 3).

These carrier dynamics are in agreement with previous TARPES investigations on BP [25, 28, 30]. Here, we focus on two open issues: BGR and VB broadening. Figure 2(d) is a zoom-in of the VB

ARPES maps at +2.4 ps delay. The energy distribution curves (EDCs) are normalized to their maxima in order to enhance the band shape. Through fitting (see section 4.1) we quantify the band dispersion, shown as open symbols. Repeating the procedure at each pump-probe delay, we can track the evolution

of the VB structure. Figure 2(e) reports the VB dispersions at three selected delays: −0.3 ps (circles), 0 ps (squares) and +2.4 ps (triangles). There is a ∼20 meV red-shift at zero pump-probe delay, and a subsequent photo-induced reduction of the band curvature at positive delay, pointing to an increased *h* effective mass. The latter is consistent with the persistent spectral enhancement at the VB sides in figure 2(b) (label 2). However, while the parabolic fit of the VB dispersion at negative delay is good (black dash line), providing a *h* effective mass $m_{VB} \sim 0.065$ m_0 (m_0 being the free *e* mass) consistent with literature [7, 25], the curves at zero and positive delays cannot be fitted by simple parabolas. This suggests two alternative scenarios: (i) loss of parabolic shape, particularly evident at positive delay, due to a flattening of the top VB (for $k_x < 0.03$ Å^{-1}), rather than increase of effective mass; (ii) pump pulses induce an upward shift (∼50 meV) of the VB toward E_F, signature of BGR [26, 27]. The flattening counterbalances the BGR on the very top of the VB.
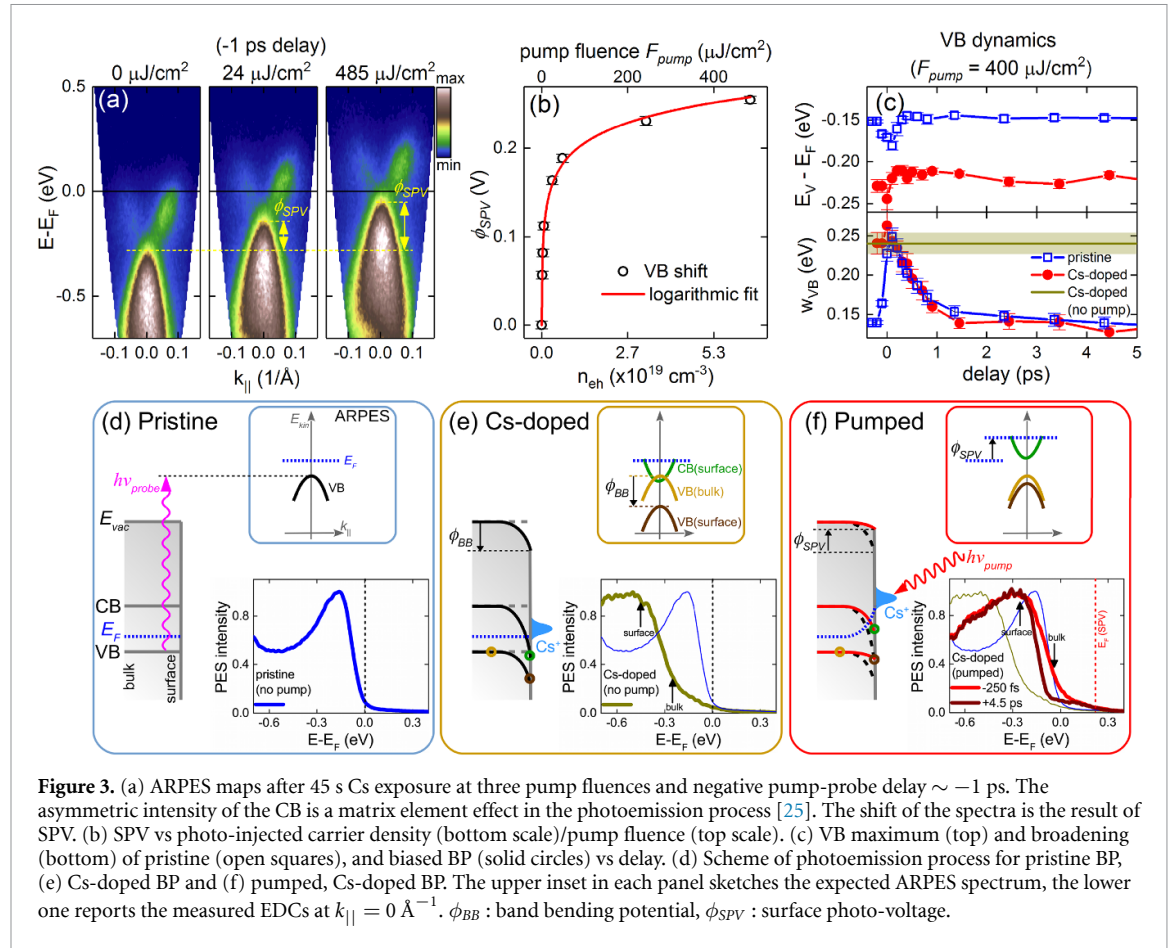
Further evidence is provided by the temporal evolutions in figure 2(f). Open squares represent the dynamics of the VB at $k_x = 0$ Å^{-1}, while solid squares refer to $k_x = 0.044$ Å^{-1} (see the corresponding dash-dotted vertical lines in figure 2(e)). A phenomenological model based on two components, labeled C1 and C2, reproduces the observed behaviors. The positive component C1 (orange dashed line) shifts the VB toward E_F and represents BGR. As photo-excited *e* and *h* rearrange in real space, their energies in the respective bands reduce as a consequence of screened exchange and correlation effects [26, 27, 46], shrinking the bandgap. This is independent of k_x, with a maximum amplitude ∼47 ± 5 meV, a rise time ∼280 ± 100 fs, and a decay time ∼4.8 ± 0.8 ps.

The negative component C2 (green dotted line) has a maximum amplitude ∼ −36 ± 5 meV, a pulsewidth-limited rise time (<100 fs) and a k_x-dependent decay (∼1 ps at $k_x = 0.044$ Å^{-1}, ∼6 ps at $k_x = 0$ Å^{-1}). To clarify its origin we evaluate the temporal evolution of the VB *intensity* by integrating the photoemission spectral weight in the small rectangular areas in figure 2(e). The result, displayed as green dots in figure 2(f), reproduces the VB transient depletion (the vertical axis on the right-hand-side of figure 2(f) shows the relative intensity I/I_0, normalized to I_0 at negative delay). There is a one-to-one correspondence with the component C2. As photo-excited carriers (*e* in CB and *h* in VB) thermalize, they fill states at the respective band edges. *h* gather at the VB maximum, as indicated by the slower intensity recovery at $k_x = 0$ Å^{-1}. *h* accumulation reduces the ARPES spectral weight and, consequently, the VB edge shifts downward to higher binding energy. Our pump fluence generates photo-carrier density $> 10^{19}$cm^{-3}, largely exceeding the equilibrium carrier concentration ∼10^{16} cm^{-3} (see section 4.2). The depletion of the VB top and the concurring

filling of the CB bottom lead to a blue-shift of the optical absorption edge, known as Burstein-Moss shift (BMS) [47, 48], caused by Pauli blocking [49]. This has been previously observed in BP, suggesting its use as active material for mid-infrared optoelectronic devices, such as tunable infrared emitters [50] and tunable optical modulators [51]. BMS and BGR can have opposite amplitudes for a given photo-carrier density [52], nearly canceling each other. The coexistence of these two compensating phenomena explains the diverging conclusions on the occurrence of BGR in BP from previous TARPES investigations [25, 28]. Our analysis confirms the presence of both BGR and BMS.

In order to understand the physics underlying the VB broadening, we analyze the photo-induced response of BP under the effect of a vertical electric bias, chemically induced by Cs adsorption. Since alkali atoms are *e* donors [53], a *n*-type surface region forms after doping, leading to band bending [54]: all energy levels bend downwards when moving from bulk to surface (it would be upwards for acceptor surface doping [54]). Owing to the giant Stark effect, in BP the CB bending is enhanced relative to VB [11, 16, 18], eventually causing surface band inversion at sufficiently high Cs coverage (>0.35 1L) [16]. Our TARPES analysis reveals that photoexcitation of Cs-adsorbed BP induces up to ∼0.25 V SPV [32, 55]. The built-in potential generated by surface doping spatially separates photo-injected *e* and *h*. With downward band bending, *e* migrate to the surface, while *h* move toward the bulk, developing a dipole field (and potential) that neutralizes the alkali-induced bending. Such dipole field can extend outside the sample, accelerating photo-emitted *e* (thus shifting all energy levels), even if they are emitted *before* pump arrival, provided they have not escaped the region in vacuum where the field spreads (see section 4.4).

Figure 3(a) shows three ARPES maps of BP measured after 45 s Cs exposure (∼0.35 1L) at *negative* pump-probe delay ∼ −1 ps and with increasing pump fluence. Without pump (left map) the Cs-induced modifications can be assessed by comparing with figure 2(a). Not only the top of the VB shifts down by ∼0.3 eV, but also the CB minimum is now roughly *touching* the VB maximum, corresponding to a downward bending ∼0.6 eV, and to the apparent closure of the gap. The middle and right maps of figure 3(a) show how increasing the pump fluence, F_{pump}, leads to a rigid, non-linear shift of the whole ARPES spectrum to higher energy, caused by SPV. Also E_F shifts accordingly. The saturation of SPV vs F_{pump} is shown in figure 3(b). The fluence on the top axis is converted into photo-injected carrier density on the bottom axis (see section 4.2) and the data are fitted by a phenomenological logarithmic model [56, 57]: $\phi_{SPV} = \alpha k_B T/e \ln(1 + n_{eh}/p_0)$. Here, $k_B T = 25$ meV is the thermal energy at RT, n_{eh} is

Figure 3. (a) ARPES maps after 45 s Cs exposure at three pump fluences and negative pump-probe delay ~ -1 ps. The asymmetric intensity of the CB is a matrix element effect in the photoemission process [25]. The shift of the spectra is the result of SPV. (b) SPV vs photo-injected carrier density (bottom scale)/pump fluence (top scale). (c) VB maximum (top) and broadening (bottom) of pristine (open squares), and biased BP (solid circles) vs delay. (d) Scheme of photoemission process for pristine BP, (e) Cs-doped BP and (f) pumped, Cs-doped BP. The upper inset in each panel sketches the expected ARPES spectrum, the lower one reports the measured EDCs at $k_{||} = 0$ Å^{-1}. ϕ_{BB}: band bending potential, ϕ_{SPV}: surface photo-voltage.

the photo-generated carrier density, $\alpha = 1.33 \pm 0.05$ and $p_0 = 2.8 \pm 0.5 \times 10^{16}$ cm^{-3} are fitting parameters (the analog of the ideality factor in a Schottky diode [57] and the equilibrium majority carrier density, respectively).

Transient photo-induced effects are reported in figure 3(c), where we compare the VB dynamics, i.e. the energy of its maximum, E_V, and the edge width, w_{VB}, deduced from the fitting procedure, before (open squares) and after (solid circles) Cs exposure, for the same excitation fluence ~ 0.4 mJ cm^{-2}. The evolution of E_V for pristine BP is the same as figure 2(f). Apart from the different binding energies, the photo-induced dynamics of the VB maximum (upper graph) before and after Cs doping are very similar. Thus, BGR and BMS appear to coexist in the biased sample as well. More challenging to understand is the dynamics of the edge width (lower graph). Photo-injection in pristine BP leads to a prompt VB broadening (w_{VB} nearly doubles within ~ 150 fs), as for Ref. [25]. In biased BP, before optical excitation, the VB width is almost twice the pristine case (dark yellow horizontal line in figure 3(c)), while after laser pumping (solid circles) it drops, closely following the dynamics in the unbiased sample.

These behaviors can be understood with the help of figures 3(d)–(f) that sketch the photoemission process under specific situations. Figure 3(d) depicts the pristine BP case. All energy levels (CB, VB, E_F, and

vacuum level, E_{vac}) are represented by horizontal lines since no band bending is present. Probe photons $h\nu_{probe}$ promote bound e from occupied VB states to free e that can travel in vacuum toward the analyzer, where the ARPES map is recorded, as sketched in the upper inset. The measured EDC at $k_x = 0$ Å^{-1} is shown in the lower inset.

Figure 3(e) shows the situation after alkali adsorption. Cs surface states are ionized donors, therefore lie above E_F. As a consequence, the n-doped surface region of the sample is characterized by the downward bending potential ϕ_{BB}. Owing to Stark effect, the CB bending is enhanced with respect to the VB one. At sufficient doping (>0.1 1L according to Ref. [16]), the minimum of the CB at the surface falls below E_F (green circle) and can be observed in static photoemission. Focusing on the VB, e photoemitted from the surface (brown circle) have the largest binding energy and determine the main peak of photoemission (see EDC in the lower inset of figure 3(e)). However, with the 6 eV photons used here, bulk sensitivity is enhanced due to the large e mean free path (~ 10 nm) [31]. Accordingly, bulk VB states (dark yellow circle) contribute to the spectral weight with lower binding energy. The enhanced VB width after Cs doping is caused by these bulk states, as sketched in the upper inset of figure 3(e), and marked by the vertical arrows in the EDC.
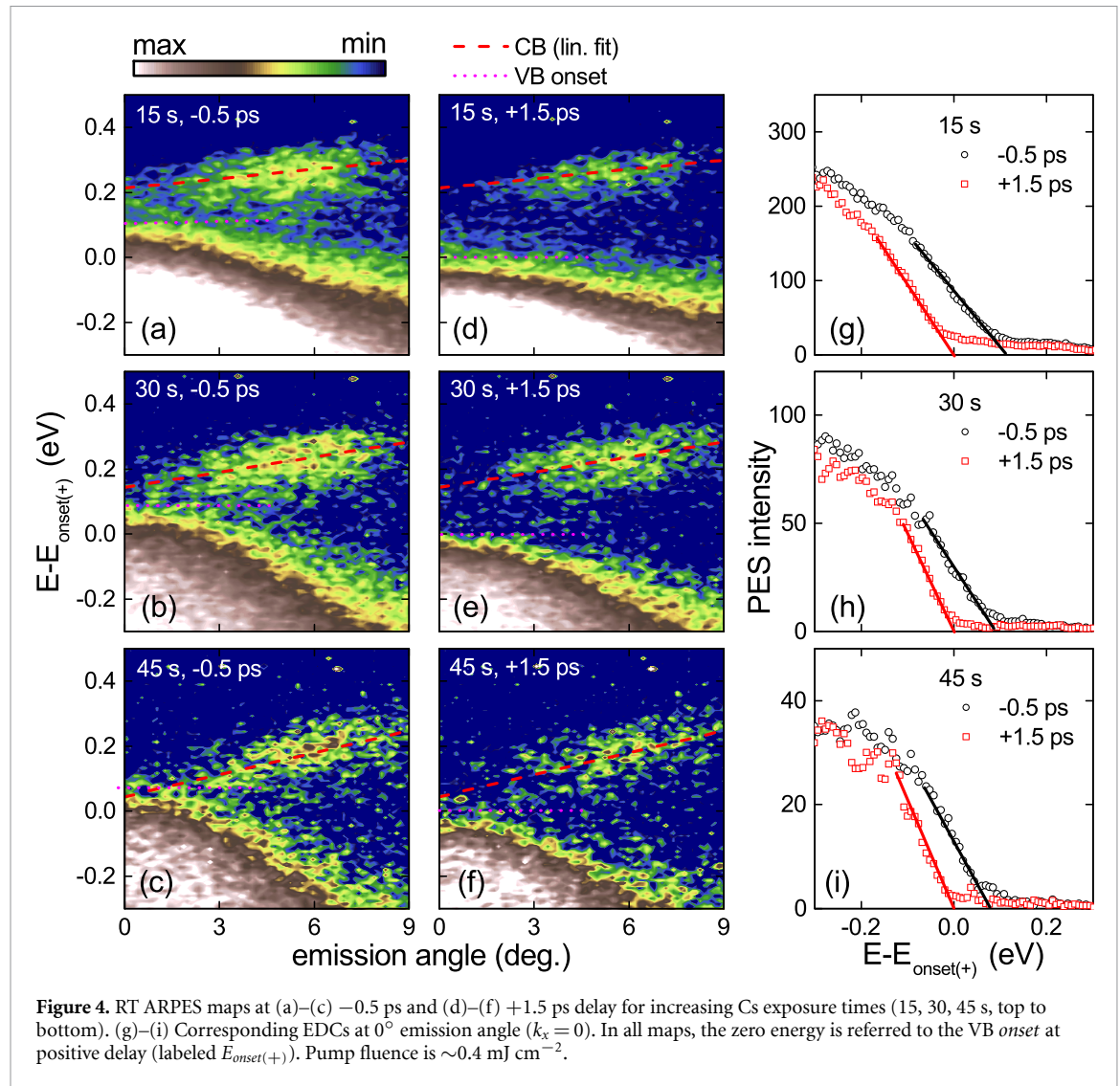
Figure 3(f) shows the pump effect on Cs-doped BP. As SPV develops, all energy levels at the surface shift upward, compensating the bending potential. Here, a distinction between negative and positive pump-probe delays must be made. If probe photons *precede* the pump pulse, *e* are emitted before SPV sets in. A few ps after pumping, the photovoltage creates a dipole field that extends in vacuum, accelerating the traveling free *e* and rigidly shifting the photoemission spectrum. Within the experimental uncertainty, the corresponding EDC is identical, apart from the energy shift, to that recorded without pump, since *e* are emitted before excitation, thus preserving the un-pumped spectral shape (as confirmed by comparing the red and dark yellow EDCs in the lower inset). Instead, at positive pump-probe delay SPV develops *before* photoemission, surface and bulk states level to similar binding energies (see upper inset) and the photoemission spectrum resembles the pristine BP case with sharper VB edge, as experimentally deduced by the dark red EDC in the lower inset. Based on these considerations, the dynamics of the VB width in figure 3(c) (red curve) represents the SPV temporal onset which, in turn, reflects the dynamics of *e*–*h* space separation that builds up the dipole field [58].

Having clarified the physical origin of the observed spectral features, we can now explain the ubiquitous photo-induced VB broadening. The close resemblance of the VB edge temporal evolution in pristine and Cs-doped samples at positive delay, figure 3(c) (bottom), points at a common mechanism, regardless of bias. Pump pulses produce identical *e* and *h* distributions that can largely exceed the equilibrium densities (see section 4.2) and decay exponentially with depth. Density gradients trigger carriers diffusion. In bulk BP, the mobility of *h* in the direction normal to the surface is larger than *e* [7]. Since mobility is proportional to the diffusion coefficient via Einstein's relation [53], *h* diffuse faster than *e*. Thus, immediately after pumping, *h* move to the bulk, leaving *e* at the sample surface even in the absence of a vertical bias. As *e* and *h* spatially separate, an outward-bound dipole field develops producing a potential, called Dember photovoltage [55], that can alter band binding energies at the surface. The build-up of this photovoltage is as fast as charge separation, and it can happen on a sub −100 fs timescale (see section 4.5). Due to the bulk sensitivity of our photoemission setup, we detect these alterations as band broadening. The orientation of the dipole field opposes the diffusion process. Eventually, charge separation (thus spectral broadening) will stop, as for figure 3(c). Further support to this explanation is provided by two experimental observations: (i) the Dember photovoltage saturates logarithmically with photo-carrier density [55] (see section 4.5) and (ii) VB broadening in pristine BP shows the same logarithmic behavior with respect to pump fluence [25].

Based on these results, the occurrence of band inversion must be cautiously claimed in biased BP. Figures 4(a)–(f) show ARPES maps recorded at negative (−0.5 ps, (a)–(c)) and positive (+1.5 ps, (d)–(f)) pump-probe delays for increasing Cs exposure times (15, 30, 45 s, top to bottom). The corresponding EDCs at $k_x = 0$ Å^{-1} are in figures 4(g)–(i). To harmonize the comparison, the zero binding energy is referred to the *onset* of the VB at positive delay (labeled $E_{\text{onset}(+)}$). Owing to the Stark effect [16, 18], as the Cs concentration increases, the CB minimum downshifts and falls within the onset of the VB at negative delay for the highest doping, reached at 45 s (figure 4(c)). This corresponds to the critical Cs coverage ∼ 0.35 1L identified in Ref. [16] at which VB and CB cross. Comparing negative and positive delays, we observe that, after photo excitation, the VB downshifts, seemingly leading to a larger bandgap. Recalling figures 3(e) and (f), this is the effect of SPV that compensates the Cs-induced bending potential. The *apparent* VB shift is due to its edge sharpening. Before pumping, the VB onset is determined by bulk states having smaller (less negative) binding energy as compared to surface states (see upper inset of figure 3(e)). After excitation, SPV neutralizes band bending, thus bulk states 'align' to surface states, appearing at larger binding energies (see upper inset of figure 3(f)) and resulting in a sharper VB edge. The crossing of VB and CB at −0.5 ps with the largest Cs dose (figure 4(c)) is the overlap of *bulk* VB and *surface* CB, resolved thanks to the bulk sensitivity of our ARPES photon energy. The CB binding energy and line shape do not significantly vary upon pumping. We only observe a loss of spectral weight after optical excitation, due to photo-induced depletion. Considering that the CB bending is more pronounced than the VB one due to the Stark effect and that SPV affects all bands equally, we should expect a well discernible photo-induced sharpening of CB at positive delay, which is not observed. The width invariance of the CB vs delay confirms its strong surface confinement, in agreement with Refs. [16–18, 21]. Thus, our data demonstrate that band crossing in chemically biased bulk BP should be claimed with caution: only in 1L or FL-BP (⩽4 layers [18]) band inversion could be seen, since bulk contributions are absent.

3. Conclusions

We employed TARPES to investigate the transient electronic dynamics of bulk BP. Our measurements show photo-induced BGR entwined to VB flattening, caused by Pauli blocking. Applying a vertical electric bias, chemically induced by Cs ad-sorption, we showed that the ubiquitous VB broadening is due to photo-carriers ambipolar drift-diffusion. Both VB and (to a larger extent) CB experience surface bending upon doping, that can be counterbalanced by a SPV prompted by laser irradiation.

Figure 4. RT ARPES maps at (a)–(c) −0.5 ps and (d)–(f) +1.5 ps delay for increasing Cs exposure times (15, 30, 45 s, top to bottom). (g)–(i) Corresponding EDCs at 0° emission angle ($k_x = 0$). In all maps, the zero energy is referred to the VB *onset* at positive delay (labeled $E_{onset(+)}$). Pump fluence is ∼0.4 mJ cm^{-2}.

This allows us to unequivocally discriminate bulk vs surface states, to establish the surface localization of the CB and to elucidate the occurrence of band inversion in bulk samples. For any application of BP involving hot carrier injection, transient changes will affect device performance. Our analysis reveals a rich and multifaceted photo-induced band dynamics that might help design opto-electronic devices. Since broad gap tunability by alkali atoms ad-soprtion has been demonstrated in transition-metal dichalcogenides [59, 60], we expect our results to be relevant to a wider class of layered materials.
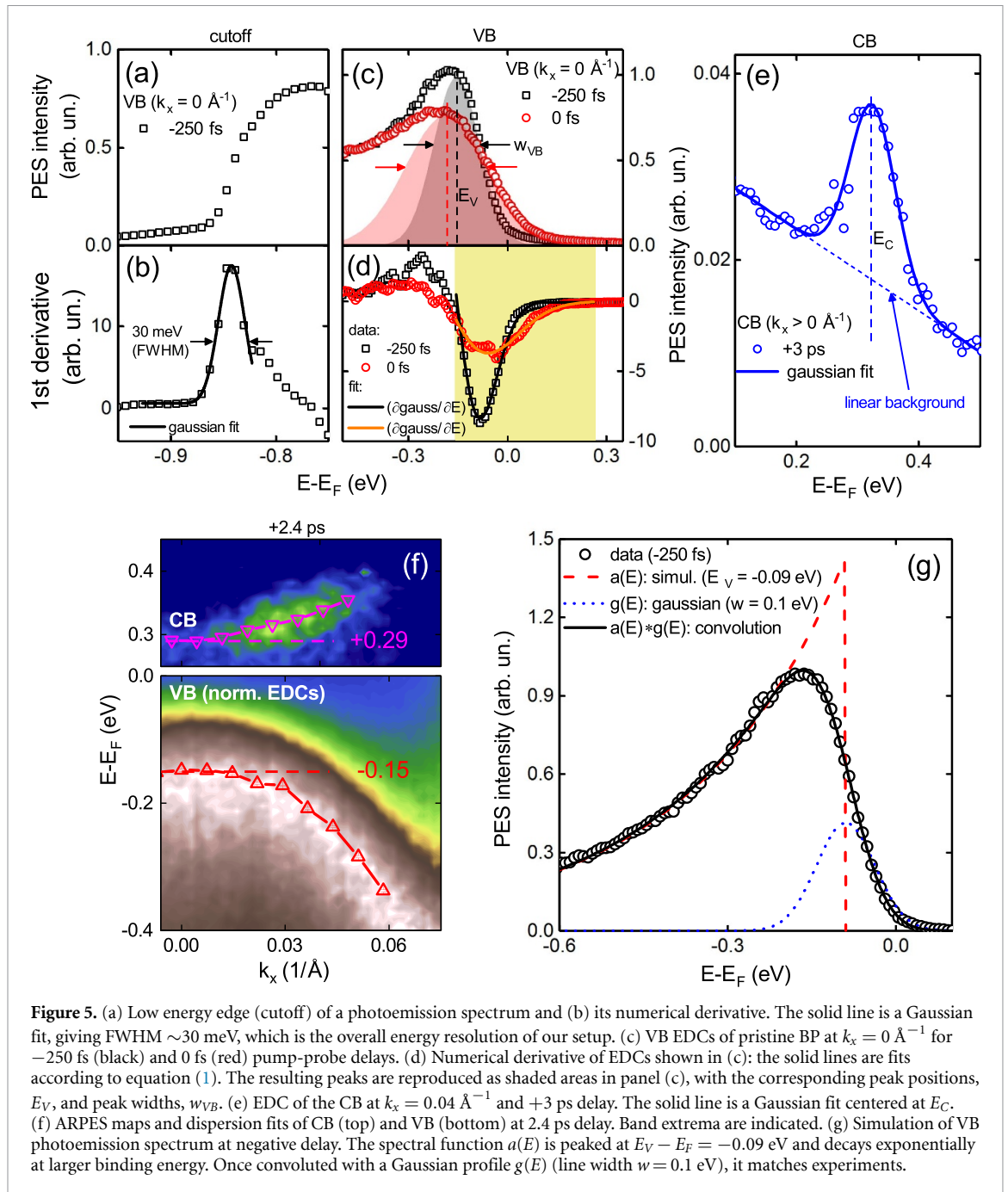
4. Methods

4.1. Spectral analysis and fitting
The overall energy resolution ΔE of our setup is ∼30 meV, as determined by the intrinsic resolution of the analyzer, and by the bandwidth of the 70 fs probe pulse. ΔE is estimated from the low energy cutoff (i.e the minimum kinetic energy) of the photoemission spectrum in figure 5(a). Its numerical derivative,

figure 5(b), fitted by a Gaussian peak gives FWHM ∼30 meV. The error bars in figures 2 and 3 are smaller than ∼30 meV because each energy position results from a fitting procedure of the EDCs that involves several (40–50) experimental points covering an energy range ∼300 meV. Figure 5(c) plots the EDCs of the VB at $k_x = 0$ Å^{-1} for −250 fs (black) and 0 fs (red) pump-probe delays. Photo-induced depletion and shift/broadening of the VB are seen. The peak asymmetry, caused by secondary e (inelastic scattering events in the photoemission process [54]), makes the exact peak identification ambiguous. Therefore, we employ a different approach. We first compute the EDCs numerical derivative, then we fit the resulting curves with the analytical derivative of a Gaussian profile:

$$\frac{\partial}{\partial E}\left[Ae^{-\frac{2(E-E_V)^2}{w_{VB}^2}} \right] = -\left[\frac{4A(E-E_V)}{w_{VB}^2} \right] e^{-\frac{2(E-E_V)^2}{w_{VB}^2}}$$

(1)

where E_V is the binding energy, w_{VB} is the width (2σ) and A is the peak amplitude. Figure 5(d) reports the

Figure 5. (a) Low energy edge (cutoff) of a photoemission spectrum and (b) its numerical derivative. The solid line is a Gaussian fit, giving FWHM $\sim$30 meV, which is the overall energy resolution of our setup. (c) VB EDCs of pristine BP at $k_x = 0$ Å^{-1} for -250 fs (black) and 0 fs (red) pump-probe delays. (d) Numerical derivative of EDCs shown in (c): the solid lines are fits according to equation (1). The resulting peaks are reproduced as shaded areas in panel (c), with the corresponding peak positions, E_V, and peak widths, w_{VB}. (e) EDC of the CB at $k_x = 0.04$ Å^{-1} and $+3$ ps delay. The solid line is a Gaussian fit centered at E_C. (f) ARPES maps and dispersion fits of CB (top) and VB (bottom) at 2.4 ps delay. Band extrema are indicated. (g) Simulation of VB photoemission spectrum at negative delay. The spectral function $a(E)$ is peaked at $E_V - E_F = -0.09$ eV and decays exponentially at larger binding energy. Once convoluted with a Gaussian profile $g(E)$ (line width $w = 0.1$ eV), it matches experiments.

results. The fits in the yellow-shaded region (40–50 experimental points) provide an accurate determination of the high-energy side of the original VB peaks, as testified by the reconstructed Gaussian profiles in figure 5(c) (colored shaded areas), and overcome the peak asymmetry issue. To deduce the VB dispersion, this procedure is repeated for various k_x. Using the Shirley method [61] to remove the incoherent background leads to very similar peak positions and widths, but poorer estimates of peak amplitude. Figure 5(e) reports the fitting routine for the CB (at $+3$ ps delay and $k_x \neq 0$ Å^{-1}, where it is more evident). In this case, the peak is modeled by a Gaussian profile with a linear background, since the spectral feature is well-defined. The CB binding energy is given by the position of the Gaussian peak (E_C). Similarly to the

VB, the CB dispersion is obtained repeating the fit at various k_x.

4.2. Electronic and optical properties of BP

Using the fitting routine previously described, we estimate the BP bandgap $E_g = 0.44 \pm 0.01$ eV, with VB maximum $\sim$0.15 eV below E_F and CB minimum $\sim$0.29 eV above E_F, see figure 5(f). Data refer to positive pump-probe delay $\sim$2.4 ps when CB is populated. This is the (VB)peak-to-(CB)peak energy gap. Refs. [28, 62, 63] suggested to use the (VB)onset-to-(CB)onset as definition of bandgap. This would give $E_g \sim 0.3$ eV. However, considering the combined energy-time resolution of our experiments, the use of band onsets underestimates the gap. On the other hand, $E_g = 0.44 \pm 0.01$ eV is slightly larger than

Table 1. *Bandgap, E_g, VB binding energy, $E_V - E_F$, intrinsic carrier density n_i, estimated h (in VB), p_0, and e (in CB) densities, n_0 at RT.*

E_g (eV)	$E_V - E_F$ (eV)	n_i (cm^{-3})	p_0 (cm^{-3})	n_0 (cm^{-3})
0.44 ± 0.01	-0.15	4.2×10^{14}	6.9×10^{15}	2.6×10^{13}
0.38	-0.09	1.4×10^{15}	7.7×10^{16}	2.6×10^{12}

the commonly reported values (0.3–0.4 eV) [64]. The discrepancy might be caused by the k_z sensitivity of photoemission, related to our photon energy. Owing to the strong band dispersion along the ΓZ crystallographic direction (see figure 1(c)), our 6 eV probe photon might correspond to a k_z slightly away from the Z-point, thus detecting a larger bandgap. We also show a VB spectral simulation assuming a Gaussian line width $w \sim 0.1$ eV, smaller than the measured one ($w_{VB} \sim 0.15$ eV), convoluted with a possible spectral function $a(E)$, figure 5(g). $a(E)$ decays exponentially at large binding energy and peaks at $E_V - E_F = -0.09$ eV. Once convoluted with the Gaussian profile, it provides an excellent fit of the experimental spectrum, placing the VB maximum at $E_V - E_F = -0.09$ eV, instead of -0.15 eV, with $E_g = 0.38$ eV.

Regardless of the exact value of E_g, equilibrium carrier concentrations in BP at RT can be estimated [65]: $n_0 = N_C e^{-(E_C-E_F)/k_BT}$ (e in CB), $p_0 = N_V e^{-(E_F-E_V)/k_BT}$ (h in VB) and $n_i^2 = n_0 p_0 = N_C N_V e^{-(E_C-E_V)/k_BT}$, with $N_C = 2.5(m_C/m_0)^{3/2} \times 10^{19}$ cm^{-3}, $N_V = 2.5(m_V/m_0)^{3/2} \times 10^{19}$ cm^{-3}. Here, E_V and E_C are the energies of the VB maximum and CB minimum, m_V and m_C the respective effective masses and n_i is the intrinsic carrier density. Due to the very similar e and h effective masses in BP ($m_C \sim m_V \sim 0.23\,m_0$) [7], we get $N_C \sim N_V \sim 2.8 \times 10^{18}$ cm^{-3}. Using the measured bandgap and VB maximum, we estimate the equilibrium e and h densities (for comparison, we use values obtained from the fitting procedure and from the convolution example of figure 5(g)) in table 1. The majority carrier density $p_0 \sim 10^{16}$ cm^{-3} agrees with that obtained from the fluence dependence of the SPV (figure 3(b)). It is instructive to compare this value with the photo-induced e–h density. According to the optical properties of BP [7], with pump photon $h\nu \sim 1.82$ eV ($\lambda \sim 680$ nm) and electric field polarized along the armchair direction, the dielectric constant is $\varepsilon \sim 12 + 2i$, which leads to refractive index $n = \sqrt{\varepsilon} \sim 3.5 + 0.3i$, reflectivity $R = (|n-1|/|n+1|)^2 \sim 0.3$ and absorption length $1/\alpha = \lambda/4\pi \mathrm{Im}(n) \sim 180$ nm [66]. The incident pump fluence F_{pump} (J cm^{-2}) can be converted into density of photo-generated e–h pairs n_{eh} (cm^{-3}) using the relation [66] $n_{eh} = F_{\mathrm{pump}}(1-R)\alpha/h\nu$ (assuming quantum efficiency of 1). Similarly, the increase of the lattice temperature can be estimated as [66]: $\Delta T = F_{\mathrm{pump}}(1-R)\alpha M/\rho c_p$, where $\rho \sim 2.7$ g cm^{-3} [67] is the mass density, $M \sim 31$ g mol^{-1} is the molar mass and $c_p \sim 21$ J mol^{-1} K^{-1} is the BP lattice specific heat [67]. With pump fluence ~ 0.5 mJ

cm^{-2} we obtain $n_{eh} \sim 7 \times 10^{19}$ cm^{-3} and $\Delta T \sim 11$ K. Although the lattice temperature is hardly affected by the laser irradiation, n_{eh} (photo excitation) $\gg p_0$ (majority carrier density). Therefore, with our laser fluence we are always in a strong electronic photo-excitation regime, and state filling effects cannot be ignored. At equilibrium, the VB is almost fully occupied and the CB empty (apart from the mild thermal carrier populations), see figure 6(a). Light illumination promotes e to the CB, leaving h in the VB. As carries thermalize, they occupy the respective band edges, figure 6(b). The resulting out-of-equilibrium charge distributions can be defined by the so-called *quasi*-Fermi levels for CB (E_{qFC}) and VB (E_{qFV}) [55, 68], both departing from the equilibrium Fermi energy, E_F [69]. State occupancy increases the optical bandgap to $E_{opt} = E_{qFC} - E_{qFV}$ (Burstein–Moss shift [47, 48], BMS, caused by Pauli blocking [70]) pushing down the VB edge. This explains the origin of component C2 in figure 2(f). Figure 6(c) sketches the combined effect of BMS and BGR: the latter shifts the VB upwards (component C1 in figure 2(f)), compensating the BMS and reducing the bandgap.

4.3. Cs ad-sorption

Cs deposition is performed with a dispenser inside the preparation chamber adjacent to the photoemission one. Control of the current through the dispenser and the residual vacuum allows reproducible results. Our sample transfer mechanism and manipulator ensure that we maintain the same relative position of the sample with respect to the dispenser after each deposition cycle. Cs adheres to the BP surface for 6–8 h without significant desorption, as verified by monitoring the BP work function during the photoemission measurements. We observe sample degradation after 24–48 h, due to Cs loss and surface contamination by the residual vacuum. The sample is cleaved *in situ* before each deposition to expose a clean pristine surface and photoemission is measured immediately afterwards.

4.4. Surface photovoltage

SPV has been extensively investigated since the early 1950s [71–74]. It is ubiquitous in doped semiconductors [75]. The basic ingredient is the presence of (intrinsic or doping-induced) surface/interface states acting as e donors or acceptors. The consequence is the formation of a space-charge layer. The resulting band bending is estimated solving Poisson's equation $\nabla^2 \phi_{BB} \propto p - n + N_D^+ - N_A^-$ (ϕ_{BB} is the built-in potential, p, n, N_D^+ and N_A^- are h, e,
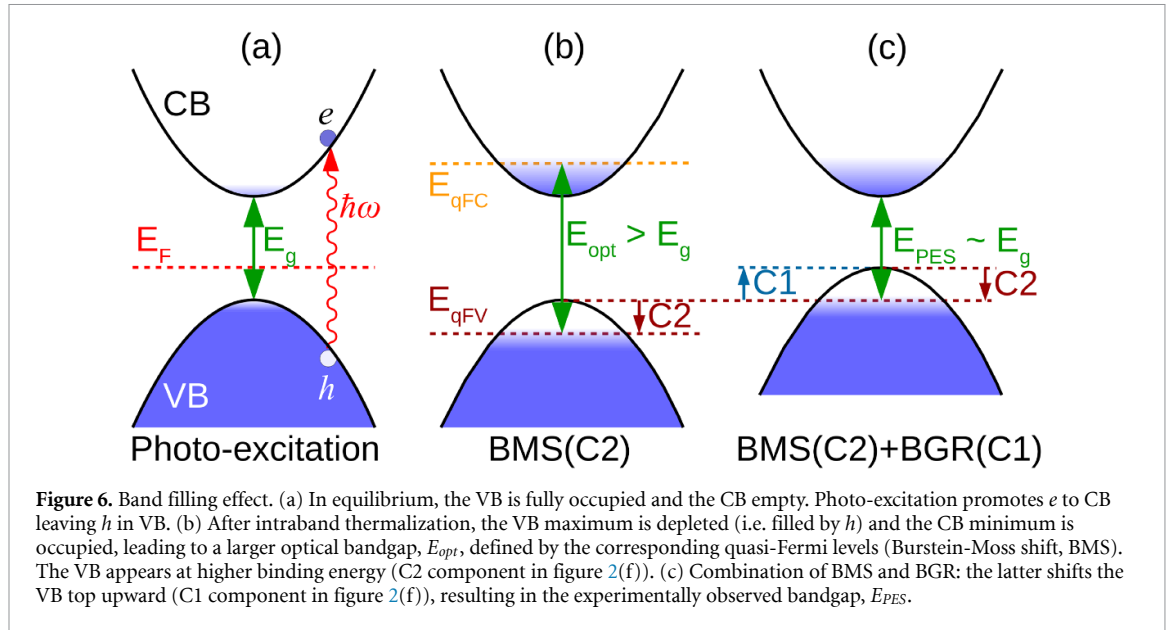
Figure 6. Band filling effect. (a) In equilibrium, the VB is fully occupied and the CB empty. Photo-excitation promotes *e* to CB leaving *h* in VB. (b) After intraband thermalization, the VB maximum is depleted (i.e. filled by *h*) and the CB minimum is occupied, leading to a larger optical bandgap, E_{opt}, defined by the corresponding quasi-Fermi levels (Burstein-Moss shift, BMS). The VB appears at higher binding energy (C2 component in figure 2(f)). (c) Combination of BMS and BGR: the latter shifts the VB top upward (C1 component in figure 2(f)), resulting in the experimentally observed bandgap, E_{PES}.

donor and acceptor densities, respectively) [75]. The width of the space-charge layer can be estimated as $L \sim \sqrt{\varepsilon_s k_B T / 2\pi e^2 n_i}$ [74]. Taking $\varepsilon_s \sim 5\varepsilon_0$ as the static permittivity of BP [76] and using the intrinsic carrier density $n_i \sim 10^{15}$ cm^{-3} previously estimated, we obtain $L \sim 30$ nm at RT. This value compares well with the expected depth sensitivity of our TARPES experiment ($\sim$10 nm). Light absorption with photon energy larger than the gap generates *e–h* pairs and the electric field in the space-charge layer spatially separates opposite charges, leading to band flattening. Band bending is *compensated* by photo-injection. This is the SPV effect. Following Ref. [55], several approaches have been developed. Here, we point out some aspects involving time-resolved photoemission techniques. The logarithmic dependence of SPV on photo-injected carrier density was suggested in Ref. [74], and adapted to time-resolved experiments in Refs. [56, 57, 77]. Although some constraints apply when dealing with time-resolved photoemission [78], the technique can provide useful information. (i) The SPV measured at negative pump-probe delay allows one to retrieve the spatial dependence of the electric field (and potential) outside the sample surface [78]. (ii) The band energy shift measured at positive delay allows one to deduce the SPV lifetime [58]. At negative delay $t < 0$, *e* are emitted *before* pump arrival. They travel in vacuum with kinetic energy $m_0 v^2 / 2$ (and velocity *v*) covering a distance $d = |vt|$ from the sample surface. At that point, the pump pulse reaches the sample and triggers SPV. The resulting dipole field (and dipole potential) extends in vacuum, accelerating the traveling electrons. The gain in kinetic energy, ΔE_{kin}, is proportional to the intensity of dipole potential ϕ at distance *d*, i.e. $\Delta E_{kin}(d) = e\phi(d)$. Therefore, mapping ΔE_{kin} vs d provides the spatial profile of ϕ in front of the surface. Figure 7(a) depicts the change of VB binding energy (relative to
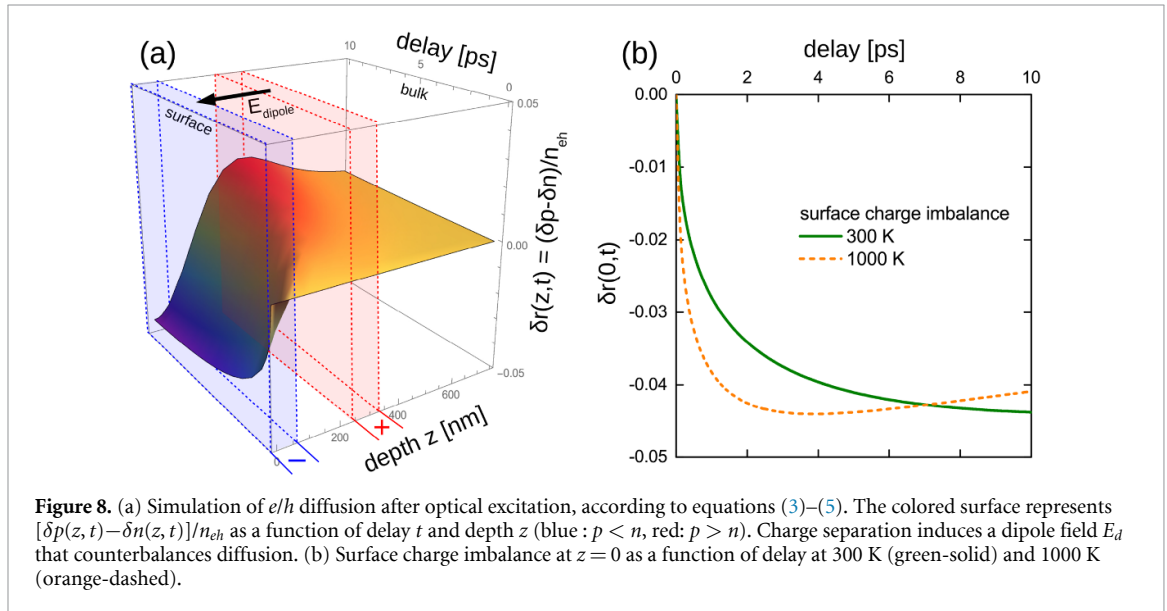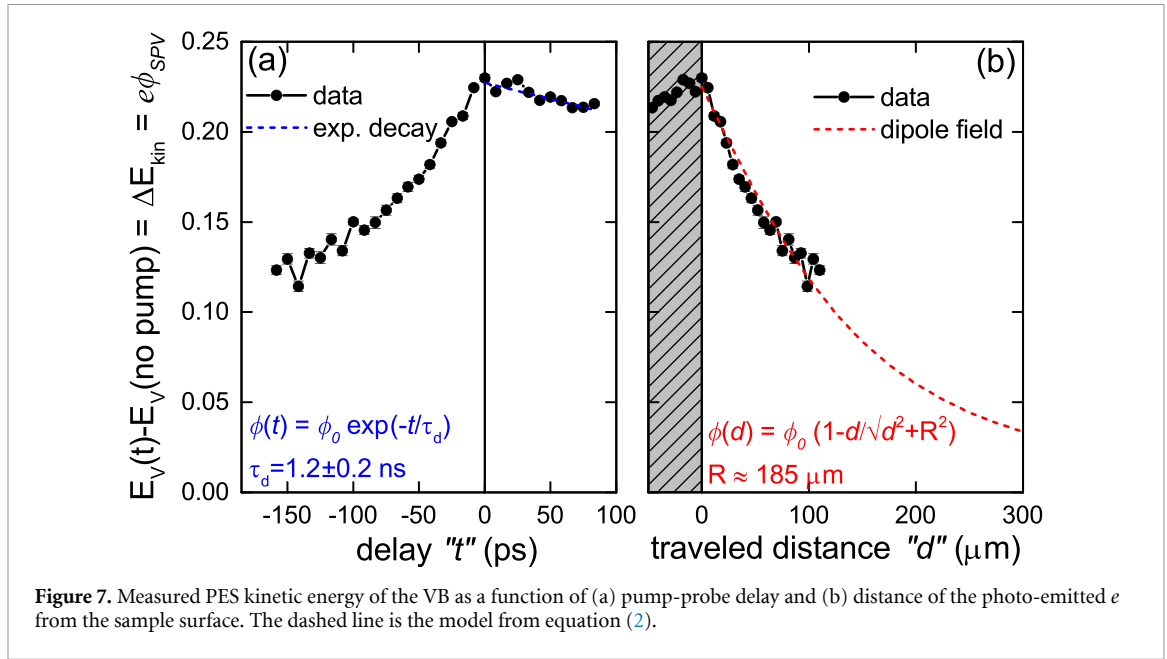
that measured *without* pump, i.e. with no SPV) in Cs-doped BP vs delay. It embodies the gained kinetic energy as a function of delay. At $t > 0$ it mildly decays, and an exponential fit provides the SPV lifetime $\tau_d = 1.2 \pm 0.2$ ns (the temporal measurement window is limited by the travel range of our delay stage). Figure 7(b) reports the same data plotted as a function of $d = |vt|$ for $t < 0$ and *v* deduced from the measured kinetic energy of the VB *without* pump. The dashed red line at $d > 0$ is the fit with ϕ generated by a uniform dipole distribution on a disc of radius *R* [78]:

$$\phi(d) = \phi_0 \left(1 - \frac{d}{\sqrt{d^2 + R^2}}\right). \qquad (2)$$

The resulting disc diameter 2*R* is $\sim$3 times larger that the pump spot size. This is due to the non-linear saturating behavior of SPV with light intensity. Even at the border of the laser spot, where the laser intensity is weaker, the SPV might be as large as in the spot center, resulting in an *apparent* disc diameter larger than the nominal laser spot size.

4.5. VB broadening in pristine BP

The pump pulse produces identical *e* (δn) and *h* (δp) distributions that can largely exceed the equilibrium densities (p_0, n_0), especially at the surface (i.e. $\delta p, \delta n \gg p_0 \gg n_0$ for *p*-doped samples), and decay exponentially with depth. The density gradient triggers carriers diffusion. For simplicity, here we will ignore recombination and drift. According to Ref. [7], in bulk BP, the *h* mobility (μ_p) along the *z*-axis, normal to the surface, is higher than that of *e* (μ_n). Since the mobility is proportional to the diffusion coefficient [53], *h* diffuse faster than *e*. Thus, after pumping, *e* tend to accumulate at the sample surface, while *h* move to the bulk. This can be simulated via diffusion equations [79]:

Figure 7. Measured PES kinetic energy of the VB as a function of (a) pump-probe delay and (b) distance of the photo-emitted *e* from the sample surface. The dashed line is the model from equation (2).

Figure 8. (a) Simulation of *e/h* diffusion after optical excitation, according to equations (3)–(5). The colored surface represents $[\delta p(z,t) - \delta n(z,t)]/n_{eh}$ as a function of delay *t* and depth *z* (blue : *p* < *n*, red: *p* > *n*). Charge separation induces a dipole field E_d that counterbalances diffusion. (b) Surface charge imbalance at *z* = 0 as a function of delay at 300 K (green-solid) and 1000 K (orange-dashed).

$$\frac{\partial \delta n(z,t)}{\partial t} = D_n \frac{\partial^2 \delta n(z,t)}{\partial z^2} \quad (3)$$

$$\frac{\partial \delta p(z,t)}{\partial t} = D_p \frac{\partial^2 \delta p(z,t)}{\partial z^2} \quad (4)$$

$$\delta p(z,0) = \delta n(z,0) = n_{eh} \exp(-\alpha|z|) \quad (5)$$

where $D_n = k_B T \mu_n / e$, $D_p = k_B T \mu_p / e$; n_{eh} and α are the photo-excited carrier density and the pump absorption coefficient, respectively. The use of the absolute value |*z*| in equation (5) ensures no diffusion through the surface. Equations (3)–(4), with initial condition given by equation (5), can be analytically solved to obtain the carrier distributions as a function of time and depth. $\delta r(z,t) = [\delta p(z,t) - \delta n(z,t)]/n_{eh}$ is

relevant for us. $\delta r > 0$ indicates *h* excess, while $\delta r < 0$ represents *e* excess. The temporal and depth evolution of $\delta r(z,t)$ are reported in figure 8(a); *e* accumulate at the sample surface within a few ps (blue color, $\delta r < 0$), while *h* move deeper in the bulk (red color, $\delta r > 0$). The estimated diffusion coefficients refer to RT. Laser pumping can induce a much higher *electronic* temperature [80], increasing the diffusion coefficient and speeding up *e* accumulation at the surface. Figure 8(b) shows the surface charge ratio δr at *z* = 0 as a function of delay for 300 K (green-solid line) and 1000 K (orange-dashed line). As *e* and *h* separate, a dipole field develops. The area marked in light blue in figure 8(a) represents the surface region of the sample with predominantly negative charge, while the light red area refers to the region where positive charge prevails. The electric dipole field E_d,

marked by the large black arrow, arises between these two regions and counterbalances charge separation. We can estimate the dipole field from current balance [79]:

$$J_n(z,t)/e = \mu_n(\delta n + n_0)E_d + D_n\frac{\partial \delta n(z,t)}{\partial z} \quad (6)$$

$$J_p(z,t)/e = \mu_p(\delta p + p_0)E_d - D_p\frac{\partial \delta p(z,t)}{\partial z}. \quad (7)$$

The field E_d that neutralizes diffusion corresponds to an overall vanishing current, i.e. $J_n + J_p = 0$, leading to:

$$
\begin{aligned}
E_d &= \frac{D_p\frac{\partial \delta p}{\partial z} - D_n\frac{\partial \delta n}{\partial z}}{\mu_p(\delta p + p_0) + \mu_n(\delta n + n_0)} \\
&\approx \frac{(D_p - D_n)\frac{\partial \delta p}{\partial z}}{(\mu_p + \mu_n)\delta p + \mu_p p_0}.
\end{aligned} \quad (8)
$$

In the last term of equation (8) we use the fact that $\delta p \sim \delta n \gg p_0 \gg n_0$ for a p-doped sample. When moving from bulk to surface, E_d builds up a potential ϕ_D, called Dember photovoltage [55]:

$$
\begin{aligned}
\phi_D &= -\int_0^\infty E_d dz \\
&= -\int_0^\infty \frac{(D_p - D_n)\frac{\partial \delta p}{\partial z}}{(\mu_p + \mu_n)\delta p + \mu_p p_0} dz
\end{aligned} \quad (9)
$$

$$= \frac{D_p - D_n}{\mu_p + \mu_n}\ln\left(1 + \frac{\mu_p + \mu_n}{\mu_p}\frac{\delta p(0,t)}{p_0}\right). \quad (10)$$

With $\mu_p = 550\,\mathrm{cm^2\,V^{-1}s^{-1}}$ [7], $\mu_n = 400\,\mathrm{cm^2\,V^{-1}s^{-1}}$ [7] and $\delta p/p_0 \sim 10^2$–10^3, we obtain $\phi_D \sim (0.8$–$1.2)k_BT/e$. A transient photo-induced electronic temperature $\sim 10^3$ K would result in $\phi_D \sim 0.1$ V, compatible with the measured VB broadening. According to equation (10), ϕ_D also saturates logarithmically with photo-injected carrier density, in agreement with Ref. [25]. Due to the absence of electric field under equilibrium conditions, the only mechanism that can transiently separate charges in pristine samples is the presence of different e/h mobilities, leading to different diffusion coefficients, as for equations (3)–(5). Such separation triggers a Dember potential (described in equation (10)), leading to VB broadening and counterbalancing further charge separation. The comparable magnitudes of SPV in biased BP and Dember potential in pristine BP explain the similar dynamics reported in figure 3(c).

Acknowledgment

ORCID iDs

A C Ferrari ⓞ https://orcid.org/0000-0003-0907-9993

E Carpene ⓞ https://orcid.org/0000-0003-3867-8178

References

[1] Qiao J, Kong X, Hu Z X, Yang F and Ji W 2014 High-mobility transport anisotropy and linear dichroism in few-layer black phosphorus *Nat. Commun.* **5** 4475

[2] Xia F, Wang H and Jia Y 2014 Rediscovering black phosphorus as an anisotropic layered material for optoelectronics and electronics *Nat. Commun.* **5** 4458

[3] Xin W *et al* 2019 Optical anisotropy of black phosphorus by total internal reflection *Nano Mater. Sci.* **1** 304

[4] Wei Q and Peng X 2014 Superior mechanical flexibility of phosphorene and few-layer black phosphorus *Appl. Phys. Lett.* **104** 251915

[5] Tran V, Soklaski R, Liang Y and Yang L 2014 Layer-controlled band gap and anisotropic excitons in few-layer black phosphorus *Phys. Rev.* B **89** 235319

[6] Rudenko A N, Yuan S and Katsnelson M I 2015 Toward a realistic description of multilayer black phosphorus: from GW approximation to large-scale tight-binding simulations *Phys. Rev.* B **92** 085419

[7] Morita A 1986 Semiconducting black phosphorus *Appl. Phys. A* **39** 227

[8] Xiang Z J *et al* 2015 Pressure-induced electronic transition in black phosphorus *Phys. Rev. Lett.* **115** 186403

[9] Fei R, Tran V and Yang L 2015 Topologically protected Dirac cones in compressed bulk black phosphorus *Phys. Rev.* B **91** 195319

[10] Liu Q, Zhang X, Abdalla L B, Fazzio A and Zunger A 2014 Switching a normal insulator into a topological insulator via electric field with application to phosphorene *Nano Lett.* **15** 1222

[11] Liu Y *et al* 2017 Gate-tunable giant stark effect in few-layer black phosphorus *Nano Lett.* **17** 1970

[12] Dolui K and Quek S Y 2015 Quantum-confinement and structural anisotropy result in electrically-tunable dirac cone in few-layer black phosphorous *Sci. Rep.* **5** 11699

[13] Deng B *et al* 2017 Efficient electrical control of thin-film black phosphorus bandgap *Nat. Commun.* **8** 14474

[14] Li Y, Yang S and Li J 2014 Modulation of the electronic properties of ultrathin black phosphorus by strain and electrical field *J. Phys. Chem.* C **118** 23970

[15] Rodin A S, Carvalho A and Castro Neto A H 2014 Strain-induced gap modification in black phosphorus *Phys. Rev. Lett.* **112** 176801

[16] Kim J *et al* 2015 Observation of tunable band gap and anisotropic Dirac semimetal state in black phosphorus *Science* **349** 723

[17] Ehlen N, Sanna A, Senkovskiy B V, Petaccia L, Fedorov A V, Profeta G and Grüneis A 2018 Direct observation of a surface resonance state and surface band inversion control in black phosphorus *Phys. Rev.* B **97** 045143

[18] Kim S-W, Jung H, Kim H-J, Choi J-H, Wei S-H and Cho J-H 2017 Microscopic mechanism of the tunable band gap in potassium-doped few-layer black phosphorus *Phys. Rev.* B **96** 075416

[19] Khoo K H, Mazzoni M S C and Louie S G 2004 Tuning the electronic properties of boron nitride nanotubes with transverse electric fields: a giant dc Stark effect *Phys. Rev.* B **69** 201401(R)

[20] Ishigami M, Sau J D, Aloni S, Cohen M L and Zettl A 2005 Observation of the giant stark effect in boron-nitride nanotubes *Phys. Rev. Lett.* **94** 056804

[21] Kiraly B *et al* 2019 Anisotropic two-dimensional screening at the surface of black phosphorus *Phys. Rev. Lett.* **123** 216403

[22] Yuan H *et al* 2015 Highly anisotropic and robust excitons in monolayer black phosphorus *Nat. Nanotechnol.* **10** 707

[23] Chen P, Li N, Chen X, Ong W-J and Zhao X 2018 The rising star of 2D black phosphorus beyond graphene: synthesis, properties and electronic applications *2D Mater.* **5** 014002

[24] Bovensiepen U, Petek H and Wolf M (eds) 2010 *Dynamics at Solid State Surfaces and Interfaces: Volume 1 – Current Developments* (Weinheim: Wiley-VCH)

[25] Chen Z *et al* 2019 Stark broadening in photoexcited black phosphorus *Nano Lett.* **19** 488

[26] Klingshirn C 2005 *Semiconductor Optics* (Heidelberg: Springer) ch 21

[27] Peygambarian N, Koch S W and Mysyrowicz A 1993 *Introduction to Semiconductor Optics* (Englewood Cliffs, N.J.: Prentice Hall) ch XIII

[28] Roth S *et al* 2019 Photocarrier-induced band-gap renormalization and ultrafast charge dynamics in black phosphorus *2D Mater.* **6** 031001

[29] Miao X, Zhang G, Wang F, Yan H and Li M 2018 Layer-dependent ultrafast carrier and coherent phonon dynamics in black phosphorus *Nano Lett.* **18** 3053

[30] Nurmamat M *et al* 2018 Prolonged photo-carriers generated in a massive-and-anisotropic Dirac material *Sci. Rep.* **8** 9073

[31] Seah M P and Dench W A 1979 Quantitative electron spectroscopy of surfaces: a standard data base for electron inelastic mean free paths in solids *Surf. Interf. Anal.* **1** 2

[32] Chen Z *et al* 2020 Spectroscopy of buried states in black phosphorus with surface doping *2D Mater.* **7** 035027

[33] Endo S, Akahama Y, Terada S and Narita S 1982 Growth of large single crystals of black phosphorus under high pressure *Japan. J. Appl. Phys.* **21** L482

[34] Ferrari A C and Basko D M 2013 Raman spectroscopy as a versatile tool for studying the properties of graphene *Nat. Nanotechnol.* **8** 235

[35] Ferrari A C 2007 Raman spectroscopy of graphene and graphite: disorder, electron-phonon coupling, doping and nonadiabatic effects *Solid State Commun.* **143** 47

[36] Kim J, Lee J-U, Lee J, Park H J, Lee Z, Lee C and Cheong H 2015 Anomalous polarization dependence of Raman scattering and crystallographic orientation of black phosphorus *Nanoscale* **7** 18708

[37] Lu J *et al* 2015 Bandgap engineering of phosphorene by laser oxidation toward functional 2D materials *ACS Nano* **9** 10411

[38] Novoselov K S, Jiang D, Schedin F, Booth T J, Khotkevich V V, Morozov S V and Geim A K 2005 Two-dimensional atomic crystals *Proc. Natl Acad. Sci.* **102** 10451

[39] Favron A *et al* 2015 Photooxidation and quantum confinement effects in exfoliated black phosphorus *Nat. Mater.* **14** 826

[40] Castellanos-Gomez A *et al* 2014 Isolation and characterization of few-layer black phosphorus *2D Mater.* **1** 025001

[41] Ribeiro H B, Pimenta M A and de Matos C J S 2018 Raman spectroscopy in black phosphorus *J. Raman Spectrosc.* **49** 76

[42] Sugai S and Shirotani I 1985 Raman and infrared reflection spectroscopy in black phosphorus *Solid State Commun.* **53** 753

[43] Boschini F, Hedayat H, Dallera C, Farinello P, Manzoni C, Magrez A, Berger H, Cerullo G and Carpene E 2014 An innovative Yb-based ultrafast deep ultraviolet source for time-resolved photoemission experiments *Rev. Sci. Instrum.* **85** 123903

[44] Shi Y, Gillgren N, Espiritu T, Tran S, Yang J, Watanabe K, Taniguchi T and Lau C-N 2016 Weak localization and electron-electron interactions in few layer black phosphorus devices *2D Mater.* **3** 034003

[45] Mao N *et al* 2019 Direct observation of symmetry-dependent electron-phonon coupling in black phosphorus *J. Am. Chem. Soc.* **141** 18994

[46] Vashishta P and Kalia R K 1982 Universal behavior of exchange-correlation energy in electron-hole liquid *Phys. Rev.* B **25** 6492

[47] Moss T S 1954 The interpretation of the properties of indium antimonide *Proc. Phys. Soc.* B **67** 775

[48] Burstein E 1954 Anomalous optical absorption limit in InSb *Phys. Rev.* **93** 632

[49] Low T, Rodin A S, Carvalho A, Jiang Y, Wang H, Xia F and Castro Neto A H 2014 Tunable optical properties of multilayer black phosphorus thin films *Phys. Rev.* B **90** 075434

[50] Whitney W S, Sherrott M C, Jariwala D, Lin W-H, Bechtel H A, Rossman G R and Atwater H A 2017 Field effect optoelectronic modulation of quantum-confined carriers in black phosphorus *Nano Lett.* **17** 78–84

[51] Lin C, Grassi R, Low T and Helmy A S 2016 Multilayer black phosphorus as a versatile mid-infrared electro-optic material *Nano Lett.* **16** 1683

[52] Feneberg M *et al* 2014 Band gap renormalization and Burstein-Moss effect in silicon- and germanium-doped wurtzite GaN up to 10^{20} cm^{-3} *Phys. Rev.* B **90** 075203

[53] Sze S M and Ng K K 2007 *Physics of Semiconductor Devices* (Hoboken: Wiley)

[54] Lüth H 2001 *Solid Surfaces, Interfaces and Thin Films* (Berlin Heidelberg: Springer)

[55] Kronik L and Shapira Y 1999 Surface photovoltage phenomena: theory, experiment and applications *Surf. Sci. Rep.* **37** 1

[56] Bröcker D, Giessel T and Widdra W 2004 Charge carrier dynamics at the SiO_2/Si(100) surface: a time-resolved photoemission study with combined laser and synchrotron radiation *Chem. Phys.* **299** 247

[57] Papalazarou E *et al* 2018 Unraveling the Dirac fermion dynamics of the bulk-insulating topological system Bi_2Te_2Se *Phys. Rev. Mater.* **2** 104202

[58] Yang S-L, Sobota J A, Kirchmann P S and Shen Z-X 2014 Electron propagation from a photo-excited surface: implications for time-resolved photoemission *Appl. Phys.* A **116** 85

[59] Kang M *et al* 2017 Universal mechanism of band-gap engineering in transition-metal dichalcogenides *Nano Lett.* **17** 1610

[60] Kim B S, Kyung W S, Seo J J, Kwon J Y, Denlinger J D, Kim C and Park S R 2017 Possible electric field induced indirect to direct band gap transition in $MoSe_2$ *Sci. Rep.* **7** 5206

[61] Shirley D A 1972 High-resolution x-ray photoemission spectrum of the valence bands of gold *Phys. Rev.* B **5** 4709

[62] Kraut E A, Grant R W, Waldrop J R and Kowalczyk S P 1980 Precise determination of the valence-band edge in x-ray photoemission spectra: application to measurement of semiconductor interface potentials *Phys. Rev. Lett.* **44** 1620

[63] Endres J *et al* 2016 Valence and conduction band densities of states of metal halide perovskites: a combined experimental-theoretical study *J. Phys. Chem. Lett.* **7** 2722

[64] Liu H, Neal A T, Zhu Z, Luo Z, Xu X, Tománek D and Peide D Y 2014 Phosphorene: an unexplored 2D semiconductor with a high hole mobility *ACS Nano* **8** 4033

[65] Ashcroft N W and Mermin N D 1976 *Solid State Physics* (Philadelphia: Saunders College)

[66] von Allmen M and Blatter A 1995 *Laser-Beam Interactions With Materials* (Berlin: Springer)

[67] Stephenson C C, Potter R L, Maple T G and Morrow J C 1969 The thermodynamic properties of elementary phosphorus the heat capacities of two crystalline modifications of red phosphorus, of α and β white phosphorus and of black phosphorus from 15 to 300 K *J. Chem. Thermodyn.* **1** 59

[68] Shur M 1990 *Physics of Semiconductor Devices* (New Jersey: Prentice Hall)

[69] Steele J A *et al* 2016 Surface effects of vapour-liquid-solid driven Bi surface droplets formed during molecular-beam-epitaxy of GaAsBi *Sci. Rep.* **6** 28860

[70] Zitter R N 1969 Saturated optical absorption through band filling in semiconductors *Appl. Phys. Lett.* **14** 73

[71] Brattain W H 1947 Evidence for surface states on semiconductors from change in contact potential on illumination *Phys. Rev.* **72** 345

[72] Brattain W H and Bardeen J 1953 Surface properties of Germanium *Bell Syst. Tech. J.* **32** 1

[73] Garrett C G B and Brattain W H 1955 Physical theory of semiconductor surfaces *Phys. Rev.* **99** 376

[74] Johnson E O 1952 Large-signal surface photovoltage studies with Germanium *Phys. Rev.* **111** 153

[75] Mönch W 2001 *Semiconductor Surfaces and Interfaces* (Berlin: Springer)

[76] Kutlu E, Narin P, Lisesivdin S B and Ozbay E 2018 Electronic and optical properties of black phosphorus doped with Au, Sn and I atoms *Phil. Mag.* **98** 155

[77] Spencer B F *et al* 2013 Time-resolved surface photovoltage measurements at *n*-type photovoltaic surfaces: Si(111) and ZnO(10 $\underline{1}$0) *Phys. Rev.* B **88** 195301

[78] Tanaka S-I 2012 Utility and constraint on the use of pump-probe photoelectron spectroscopy for detecting time-resolved surface photovoltage *J. Electron Spectrosc. Relat. Phenom.* **185** 152

[79] McKelvey J P 1966 *Solid State and Semiconductor Physics* (New York: Harper and Row)

[80] Carpene E 2006 Ultrafast laser irradiation of metals: beyond the two-temperature model *Phys. Rev.* B **74** 024301